Biomedical Physics & Engineering Express

RECEIVED
16 September 2016

REVISED
14 October 2016

ACCEPTED FOR PUBLICATION
7 November 2016

PUBLISHED
20 January 2017

PAPER

An improved extended Kalman filter for diffuse optical tomography

G R Baez[1], J A Pomarico[1] and G E Elicabe[2]

[1] Biomedical Optics Group, Centro de Investigaciones en Física e Ingeniería del Centro de la Provincia de Buenos Aires, CIFICEN (UNCPBA-CICPBA-CONICET), Tandil-Argentina
[2] Instituto de Investigaciones en Ciencia y Tecnología de Materiales, UNMDP-CONICET, Mar del Plata-Argentina

E-mail: gbaez@exa.unicen.edu.ar

Keywords: imaging through turbid media, light propagation in tissues, medical and biological imaging, diffuse optical tomography, extended Kalman filter

Abstract

In diffuse optical tomography (DOT) the main objective is to estimate the absorption coefficent and the reduced scattering coefficient of a certain media given a set of boundary measurements. Biological tissues contains many objects such as arteries, skin and fat whose optical properties are rather different than those of the media. When these values are near to those of the background, linear techniques are usually used to estimate them. However, certain objects, such as tumors, may have properties which cannot be well estimated with linear models. In this article we present a non-linear approach for the frequency-domain problem based on an improvement of the extended Kalman filter (EKF) which is used in estimation-observation problems, and modified to the DOT parameter estimation problem. The EKF allows to incorporate prior information of the measurement noise as well as certain characteristics of the objective media. We show that the proposed methodology is equivalent to existing methods but can be applied to other schemes such as model reduction as suggested in previous works. Some computer simulations as well as experimental results are shown to validate our proposal.

1. Introduction

Diffuse optical tomography (DOT) is an imaging technique that allows one to recover, given boundary measurements, the optical properties within a turbid medium. Many applications of this technique are in the field of medical imaging [1]. Given that the inverse problem needed to solve DOT is computationally expensive, many works have been done considering linear approximations, for example in [2] the linear problem is solved with the use of prior anatomical information, or, in [3], validates experimentally a hierarchical Bayesian problem, corresponding to the linear case. However, there are not so many contributions for the non-linear case [4, 5], where a Levenberg–Marquardt algorithm and a Gauss–Newton scheme were developed, respectively.

The Kalman filter (KF) [6] is a technique used to solve observation-estimation problems which has been used in many areas of science and engineering. As it has been so widely studied, many improvements and implementations have been developed succesfully (see for example [7]). In DOT, the KF was applied to model physiological components from physiological measurements [8]. Although, the extended Kalman filter (EKF) has been applied in fluorescence diffuse optical tomography (FDOT) to study the pharmacokinetics of the indocyanine green [9, 10], to the best of the autors knowledge, it has not been applied, so far, to DOT.

In this work, we present a modified EKF algorithm, which is one of the possible extensions to non-linear problems, in the context of DOT. This contribution is organized as follows: in the next section we present the theoretical basis of the DOT problem and the chosen modeling approach. Then, in section 3, the EKF algorithm and a the proposed modification are described. In section 4, we present the rationale and algorithms for optical properties estimation. Section 5, describes the validation of the proposal through numerical simulation and phantom experiments. The main results are shown in section 6. Finally, in section 7 we present a discussion together with the main conclusions.

2. Light propagation through diffusion equation

Light propagation in turbid media, such as biological tissues, is modeled with the radiative transfer equation (RTE) [11], which is an integro-differential equation whose solutions are available only for simple and homogeneous geometries [12, 13]. Numerical or stochastic methods such as Monte-Carlo integration are possible but they are computationally too expensive if they are meant to be applied in clinic evaluation; requiring quasi real-time performance. To avoid these problems, a diffusion approximation of the RTE can be derived [14] through spherical harmonics expansion and considering only isotropic and linearly anisotropic terms Consider $\Omega \subset \mathbb{R}^n$ be a simply connected domain with boundary $\partial\Omega \subset \mathbb{R}^n$. Let $\mu_a(r)$ and $D(r)$ be two scalar functions representing the absorption and diffusion coefficients at position r, respectively. Let $S(r, \Omega)$ be an incoming radiation boundary condition at position r with modulation frequency Ω. Then, the photon density $I(r, w)$ inside the domain satisfies the equations [15]

$$\begin{cases} \nabla \cdot (D(r) \cdot \nabla I(r, w)) - \mu_a(r) I(r, \Omega) = 0, & r \in \Omega/\partial\Omega \\ I(r, w) + 2AD(r)\frac{\partial I}{\partial \hat{n}} = S(r, \Omega), & r \in \partial\Omega \end{cases} \quad (1)$$

where $D(r) = \frac{1}{3(\mu_a(r) + \mu_s'(r))}$ with $\mu_s'(r) = \mu_s(1 - g)$ is the reduced scattering coefficient and g the anisotropy factor. A is the Fresnel reflection coefficient which incorporates the refractive index mismatch at the air-tissue boundary. $\hat{n}$ is the outward normal vector to Ω.

The solution of equation (1) is modeled with an operator $F : X \to Y$ where X is the space of parameters (μ_a, D) and Y is the measurement space. There are many approaches to F, such as analytical results [17, 18, 16] when the media is homogeneous and the geometry is simple, or numerical results (finite difference [14], finite element [4, 5], Monte Carlo solutions [19]) otherwise. In this work we use NIRFAST [4] finite element approach, which is a MATLAB® toolbox for DOT that solves the forward problem, the inverse problem and also calculates the Fréchet Derivative, or Jacobian matrix, which will also be used throughout this article.

3. The EKF

The KF [20] is a tool that allows one to perform dynamic estimation-observation in dynamic systems, based on Gaussian likelihood and Gaussian *a priori* information. In linear dynamic systems it can be shown that the solution obtained with this filter is optimal, provided that some conditions are satisfied [6].

The EKF is the natural extension of the linear KF [6] to non-linear problems. The main idea is to take the linearization at each time step and apply the linear KF to predict and update the state towards the next time step.

The general formulation can be stated as follows: let $x_k \in \mathbb{R}^n$ be the estimated parameter and $y_k \in \mathbb{R}^m$ the measurement obtained, both at k–time, the observation-evolution model is

$$\begin{cases} x_{k+1} = M_k(x_k, u_k) + w_k & w_k \sim N(0, Q_k), \\ y_{k+1} = H_k(x_k, u_k) + r_k & r_k \sim N(0, R_k) \end{cases} \quad (2)$$

where M_k is the state evolution operator, H_k is the measurement operator, u_k is a control variable, $Q_k \in \mathbb{R}^{n\times n}$ and $R_k \in \mathbb{R}^{m\times m}$ are positive-semidefinite matrices and $N(a, C)$ is a Normal distribution with mean a and covariance matrix C. Given $x_0^+ = E(x_0)$, $P_0^+ = E((x_0 - x_0^+)^\mathsf{T}(x_0 - x_0^+))$, where $E(x)$ is the mathematical expectation, the EKF solution to the system (2) is given by a prediction-update procedure accordingly with [6]

Prediction

$$\begin{aligned} P_k^- &= M_{k-1}' P_{k-1}^+ (M_{k-1}')^\mathsf{T} + Q_{k-1} \\ x_k^- &= M(x_{k-1}^+, u_{k-1}) \end{aligned} \quad (3)$$

Update

$$\begin{aligned} K_k &= P_k^- H_k'^\mathsf{T} (H_k' P_k^- H_k'^\mathsf{T} + R_k)^{-1} \\ x_k^+ &= x_k^- + K_k[y_k - H(x_k^-)] \\ P_k^+ &= (I - K_k H_k') P_k^- \end{aligned} \quad (4)$$

where $M_{k-1}' = M_{k-1}'(x_{k-1}^+, u_{k-1})$ and $H_{k-1}' = H_{k-1}'(x_k^-)$ and $M'(x^*) = \frac{\partial M}{\partial x}\Big|_{x = x^*}$.

At each time step, the predicted or *a priori* covariance P_k^- is estimated by linearizing the state evolution operator and combining it with the *a posteriori* estimate P_{k-1}^+ obtained at the last time step. The predicted estimate x_k^- is obtained by evolving the *a posteriori* estimate with the operator M. In the update phase, Kalman gain matrix K_k is calculated. This matrix tells us how reliable the measurements are. The *a posteriori* estimate x_k^+ is an update that considers the Kalman gain and the innovation term $(y_k - H(x_k^-))$.

Even though the EKF is the natural extension of the linear KF, it does not preserve the optimality property because of linearization errors and the Gaussian assumption [6].

4. Optical properties estimation

Consider the frequency-domain problem of estimating $x = (\mu_a, D)$, $x \in \mathbb{R}^{2n}$ with n the number of discrete objects in our medium. Given a modulation frequency Ω, at each detector, amplitude and phase are obtained in a complex measurement, i.e. $y \in \mathbb{C}$, $y^{p,j} = y_{\text{amp}}^{p,j} + \text{i}y_{\text{phase}}^{p,j}$, where $p = 1,.., n_s$, $j = 1, \ldots, n_d$, where p and j are the source and detector numbers, respectively. The integers $m = 2 * n_s * n_d$ are the total numbers of sources and detectors,

respectively. In this way we get $y \in \mathbb{R}^m$ which represents the measurements. If we define

$$\tilde{y} = \log(\hat{y}^{\text{amp}}, \hat{y}^{\text{phase}}), \tag{5}$$

where the logarithm is to be applied component-wise, and

$$\hat{y}^{\text{amp}} = (y^{1,1}_{\text{amp}}, \ldots, y^{ns,nd}_{\text{amp}}) \tag{6}$$

$$\hat{y}^{\text{phase}} = (y^{1,1}_{\text{phase}}, \ldots, y^{ns,nd}_{\text{phase}}). \tag{7}$$

In order to use the EKF model we need to write the estimation problem as an observation-evolution model. Since we are considering optical parameters, we assume no evolution. Thus, we consider $M_k(x, u) = x$; if we put it in terms of (2) we obtain

$$x_{k+1} = x_k + w_k$$

which is a random walk, i.e. the difference between the next and present steps follows a normal distribution with zero mean.

Let $Q_k = Q$ and $R_k = R$ for all k, i.e. the covariances are time-independent, and $H = F$ the model in (1). Finally, we set all the measurements to be the one and only measurement we have, i.e. $y_k = y$ for all k. We are ready to implement the EKF approach obtaining algorithm 1.

Algorithm 1. Extended Kalman filter

Let H, Q, R be as defined above, let
$x_0^+ = E(x_0)$, $P_0^+ = E((x_0 - x_0^+)^{\intercal}(x_0 - x_0^+))$
Procedure EKF(x_0^+, P_0^+, Q, R) ▷ *A priori* information
  While stopping criteria is not satisfied **do**
    Calculate Jacobian $H'(x_{k-1}^+)$
    Calculate the predicted parameters x_k^- and P_k^- according to equation (3)
    Calculate the *a posteriori* parameters x_k^+ and P_k^+, using equation (4)
    $k = k + 1$
  end while
  return x_k^+, P_k^+
end procedure

However, this approach, depending on the parameters Q_k and R_k, could take a large amount of iterations making the method inefficient. To improve convergence we add a line search when we calculate the *a posteriori* estimate, i.e. we seek for a $\alpha^* \in \mathbb{R}$ such that

$$\alpha^* = \arg\min_{\alpha \in \mathbb{R}} (||D(H(x_k^- + \alpha\delta_k)) - y||_2^2 + ||L(x_k^- + \alpha\delta_k)||_2^2) \tag{8}$$

where $\delta_k = K_k[y_k - H(x_k^-)]$, as defined in (4), $R_k = DD^{\intercal}$ and $P_k^+ = LL^{\intercal}$, which can be obtained via a Cholesky factorization [21]. From an optimization point of view, we are considering vector δ_k as a descent direction, the line search approach finds a better estimate given the actual point x_k^- and δ_k.

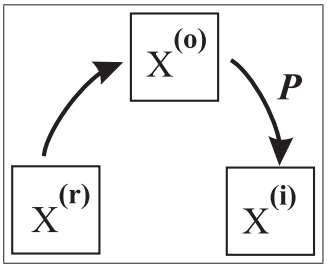

Figure 1. Mesh transformation scheme. X^r refers to the regular mesh, X^o corresponds to the original mesh, and x^i refers to the reduced mesh. $P : \mathbb{R}^n \to \mathbb{R}^m$ is the transformation from the original mesh to the reduced mesh.

Inexact line search such as polinomial interpolation or Armijo rule, can be used [22].

With this improvement, the algorithm is modified obtaining the improved EKF

Algorithm 2. Improved EKF

Let H, Q, R be as defined above, let
$x_0^+ = E(x_0)$, $P_0^+ = E((x_0 - x_0^+)^{\intercal}(x_0 - x_0^+))$
Procedure EKF(x_0^+, P_0^+, Q, R) ▷ *A priori* information
  $k = 1$
  While stopping criteria is not satisfied **do**
    Calculate Jacobian $H'(x_{k-1}^+)$
    Calculate the predicted parameters x_k^- and P_k^- according to equation (3)
    Calculate K_k, P_k^+, and $\delta_k = K_k[y_k - H(x_k^-)]$
    Perform a line search by solving (8) and update $x_k^+ = x_k^- + \alpha^* K_k[y_k - H(x_k^-)]$
    $k = k + 1$
  end while
  return x_k^+, P_k^+
end procedure

4.1. Acceleration via model reduction

A drawback of the method is the computational burden, considering that an inversion must be computed, and several matrix products are needed to update the covariance matrices. One possible solution to this issue is to reduce the size of the mesh in such a way that the computation can be made fast enough to satisfy the required application, for example, in real-time monitoring where the update must be done in the order of 2 or 3 s. To do so, we propose to use a Model Reduction approach as suggested in [23]. First, the unstructured mesh $x^{(o)}$ is interpolated into a regular mesh $x^{(r)}$, where we can define the first order derivative L and use it to generate the gaussian smoothed samples $\{x_1^{(r)}, x_2^{(r)}, \ldots, x_k^{(r)}\}$, then, the samples are taken back to the original mesh $\{x_1^{(o)}, x_2^{(o)}, \ldots, x_k^{(o)}\}$ and taken to a reduced mesh $\{x_1^{(i)}, x_2^{(i)}, \ldots, x_k^{(i)}\}$ via an application $P : \mathbb{R}^n \to \mathbb{R}^m$, as seen in figure 1.

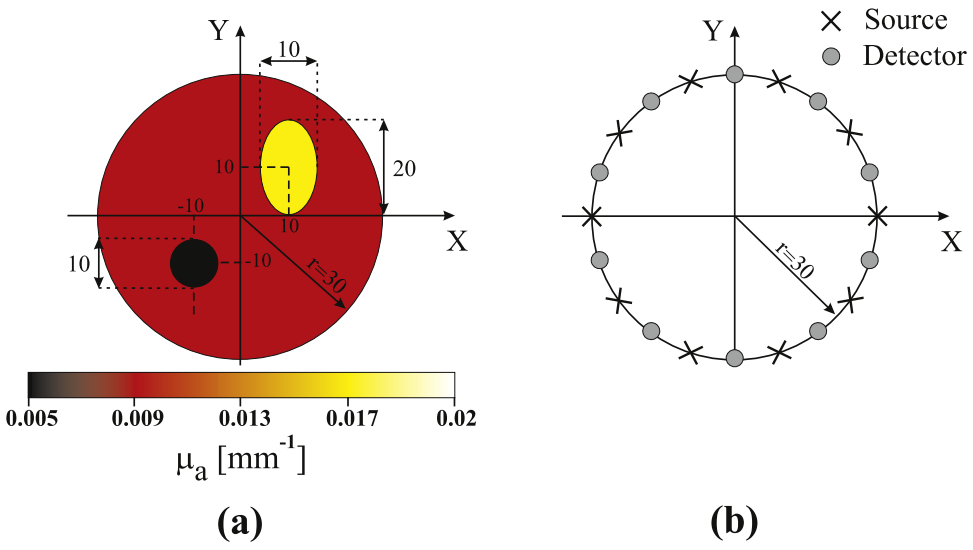

Figure 2. First scenario: (a) domain and (b) source–detector configuration. All dimensions in mm.

Following the procedures in [23], the mean Model Reduction error $e_0 = E(H(x^{(o)}) - H(x^{(r)}))$, where E is the mathematical expectation, and the corresponding covariances matrices Γ_{x_h} and Γ_H are implemented in our EKF by setting

$$\hat{y}_0 = \hat{y} - e_0 \tag{9}$$

$$P_0 = P_0 + \Gamma_{x_h} \tag{10}$$

$$R = R + \Gamma_H \tag{11}$$

This is an example of the potentiality of the EKF formulation, allowing to implement Model Reduction in a natural scheme, it is possible to perform a very fast implementation in MATLAB® which can be improved even more if languages such as C or FORTRAN are used to develop such schemes.

5. Validation

To validate our approach, we performed both, computational simulations and phantom experiments.

5.1. Computational simulations

As a proof of concept, continous-wave (CW) simulations (the modulation frequency set to $\omega = 0$) carried out in a 2D domain containing embedded objects with optical properties emulating a tumor [24] were used to generate synthetic measurement sets. They were contaminated with measurement noise at different levels. These data sets were used to reconstruct the optical properties of the whole domain. The quality of the reconstructions obtained using our EKF were compared with those found with the NIRFAST solver [4] by means of the merit criterium given below. In the first scenario, the computational domain consists of a circle of radius $r = 30$ mm, as shown in figure 2 with background optical properties $\mu_a^0 = 0.01$ mm^{-1} and $\mu_s'^0 = 1$ mm^{-1}. Two objects are embedded inside the medium, namely, a disk with $\mu_{a_{\text{disk}}} = \mu_a^0/2$ centered at $r_{\text{center}_{\text{disk}}} = [-10\text{ mm}, -10\text{ mm}]$ with radius $r_{\text{dsk}} = 5$ mm, and an ellipse with $\mu_{a_{\text{ell}}} = 2\mu_a^0$ centered at $r_{\text{center}_{\text{ell}}} = [10\text{ mm}, 10\text{ mm}]$ with major and minor semi-axis lengths of 10 mm and 6 mm, respectively.

The reconstruction bi-dimensional mesh is compound of 2907 nodes and 5624 triangular elements, while the mesh used to generate data is compound of 10547 nodes and 20404 elements; the sources and detectors are uniformly placed over the domain boundary as shown in figure 2. If we assume multiplicative noise, when we take the logarithm of the measurements, the noise is additive.

$$\log y_{\text{data}} = \log y_{\text{model}} + \log y_{\text{noise}}, \tag{12}$$

where y_{noise} takes account of all the noise sources such as shot noise, detector coupling, source attenuation, electronic noise, etc. For our simulations, the noise level is set between 1.01 and 1.05 obtaining from 1% to 5% of deviation.

To show the proposed acceleration, we performed the same reconstruction with Model Reduction using a coarse mesh with 341 nodes and 618 triangular elements which, in normal conditions, would give erroneous results, in this work, we have used $n = 2000$ Gaussian smoothed samples.

5.2. Phantom experiment

As sketched in figure 3 a parallelepiped of height and width given by $h = w = 100$ mm and thickness $L = 33$ mm, made of epoxy resin was used as a phantom to acquire time-resolved (TR) data using a time correlated single photon counting system (Becker&Hickl, SPC 130). TiO_2 particles and black tonner were added to the resin to provide the desired scattering and absorptionvproperties simmilar to those of biological tissues, respectively. The optical properties of the homogeneous background at

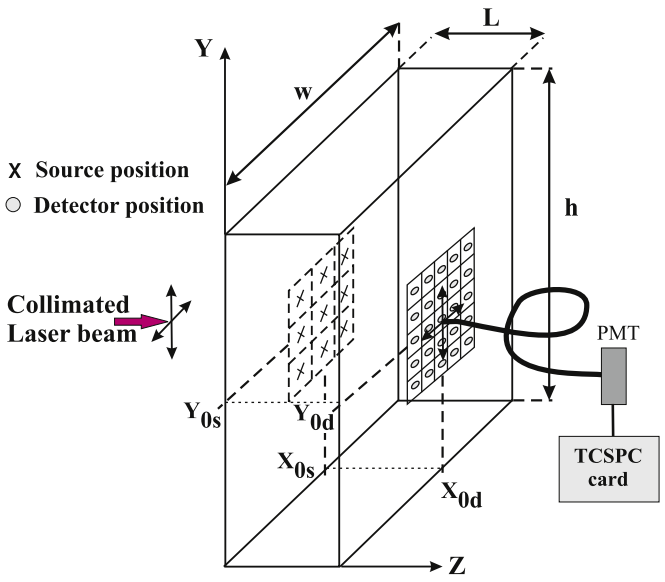

Figure 3. Experimental Setup showing the host parallelepiped and the areas scanned by the source and detection fiber bundle. Inclusions are not shown for clarity.

$\lambda = 785$ nm were obtained from TR measurements, resulting in $\mu_a^0 = 0.003342\,\text{mm}^{-1}$ and $\mu_s'^0 = 2.5833\,\text{mm}^{-1}$. Two cylindrical inclusions of radius and height of 10 mm, emulating tumor-like lesions and also made of epoxy resin were embedded in the host phantom, located at $(x_1, y_1, z_1) = (8, -10.5, 7.5)$ mm for inclusion 1 and $(x_2, y_2, z_2) = (0, 0, 23)$ mm for inclusion 2. Their optical properties were previously measured from corresponding homogeneous slabs from which the inclusions were cut and shaped. Their values relative to the host resulted: $\mu_a^1 = 2.5\mu_a^0$, $\mu_s'^1 = 1.5\mu_s'^0$, $\mu_a^2 = 1.8\mu_a^0$ and $\mu_s'^2 = 1.8$

The phantom was illuminated at one face by a collimated laser beam emmited from a 4 mW average power *ps* diode laser operating at $\lambda = 785$ nm and at 50 MHz repetition rate (Becker & Hickl BHLP-700). Diffuse light emerging at the opposite flat face of the host was collected by an optical fiber bundle ($\phi = 4$ mm, NA: 0.11) and sent to the photomultiplier (Becker& Hickl, PMC 100).

The illuminating beam was positioned in directions X and Y around nine positions, centered at $(X_{0s}, Y_{0s}, Z_{0s}) = (0, 0, 0)$, uniformly covering a flat window of 20×20 mm^2 in 10 mm steps in both directions. Similarly, the collection fiber bundle was moved around 25 positions on the light exit face, uniformely covering the same area as the laser, but in 5 mm steps and centerd at $(X_{0d}, Y_{0d}, Z_{0d}) = (0, 0, L)$.

The whole system was automated by an ad-hoc software written in LabView® and using motorized translation stages (Zaber Technologies, Canada). Data was collected in time-domain regime, Fourier transformed to the frequency-domain, and selected the amplitude and phase corresponding to $\omega = 100$ MHz, in order to be handled by our algorithm. Calibration was performed using and homogeneous phantom with the same dimensions and optical properties as the background of the objective phantom. Calibration is necessary to make the measurements compatible with the algorithm. The reconstruction mesh is an unstructured parallelepiped mesh with 11877 nodes and 49633 linear tetrahedral elements. The reconstruction volume simulates a subdomain of the original phantom of dimensions 45 mm $\times$ 45 mm $\times$ 33 mm (see figure 4).

6. Results

In order to perform the reconstructions detailed in algorithm 2, we choose as starting values $x_0^+ = \mu_a^0$, $P_0^+ = \text{diag}(\gamma)$ with $\gamma = 10^{-3}$. We set the covariance with a short step to avoid very large jumps which could lead to divergence of the method because of the ill-posedness of the problem. To initialize R we use $R = \text{diag}(1/|y_{\text{data}}|)$ (as suggested in [25]) where we assume the that measurements are uncorrelated. Note that the measurement covariance acts as a measurement regularization operator (see equation (4)), because of this, high diagonal elements in the covariance matrix could lead to smooth solutions at the expense of the quality of the reconstruction setting. $R = 0$ is equivalent to assume that the measurements are perfect, i.e. without noise, which could lead to noisy reconstructions because the operator H_k is ill-conditioned [14]. The algorithm stops when the norm of the relative step is below 2%. Given that the linear KF, in the Bayesian sense is the Maximum a Posteriori (MAP) [26] estimate of a Gaussian likelihood over the measurement error and a Gaussian *a priori*, the EKF is the MAP calculated at each iteration, also assuming

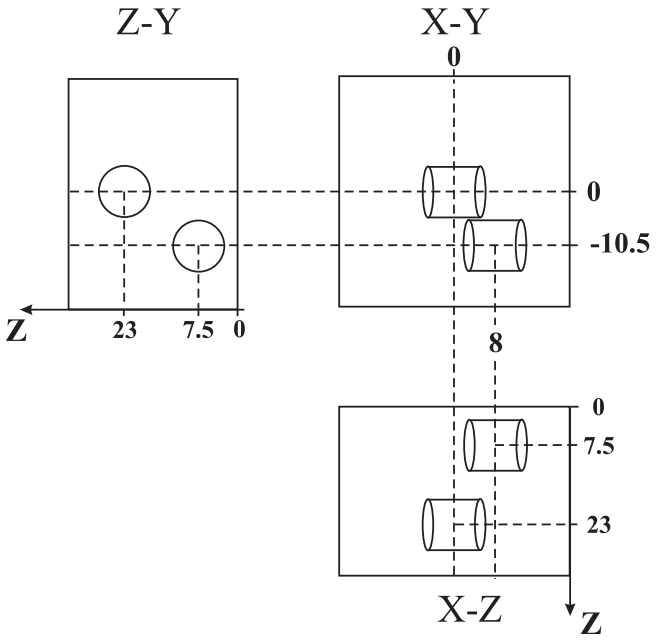

Figure 4. Geometry of the phantom sub-domain showing the locations of the two target inclusions. The sub-domain shown has dimensions 45 mm × 45 mm × 33 mm.

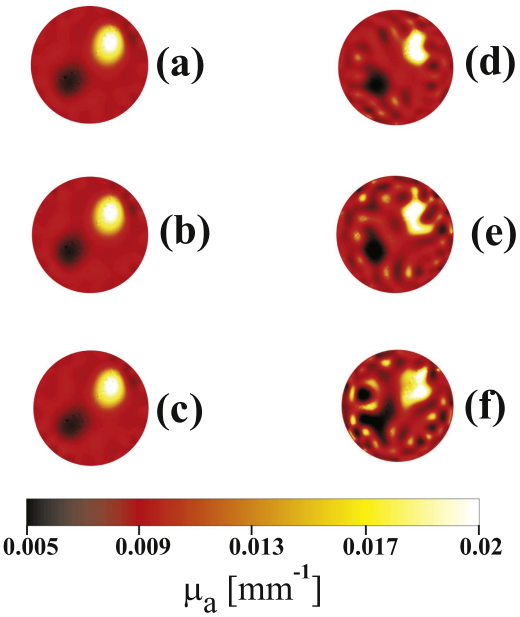

Figure 5. Simulated data reconstruction: comparison of μ_a EKF reconstructions (first column) versus μ_a NIRFAST reconstructions (second column) for three different noise levels. Namely, from top to bottom, 0.5%, 1% and 2%. No filtering was used between iterations in any case.

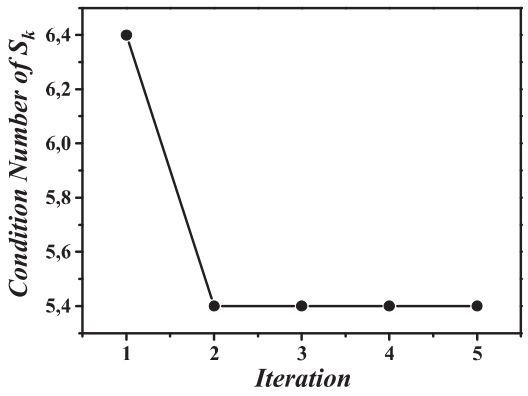

Figure 6. Condition number of the matrix $S_k = H_k' P_k^- H_k'^{\mathsf{T}}$ in the non-reduced mesh, for a 3% noise level versus iteration number.

Gaussian likelihood and prior, which guarantees smooth solutions as shown in figure 5. To assess the goodness of the reconstructions we use the merit function defined by

$$e(x_{\text{rec}}) = ||x_{\text{rec}} - x_{\text{exact}}||_2 / ||x_{\text{exact}}||_2 \qquad (13)$$

where x_{exact} is the objective mesh. In figure 5 reconstructions of scenario 1 corresponding to figure 2 are shown where the NIRFAST reconstruction is used as a reference. Note that NIRFAST offers two types of iteration-based filters, namely, a median and a mean type. No filtering was used in our simulations and comparisons given that our algorithm does not make use of any filter. To test the robustness of our approach, three different noise levels are represented. Namely, the first row corresponds to a noise level of 0.5%, the second one to noise level of 1% and the third one to 2%. Although both algorithms successfully locate both inclusions, below 2% of noise level, the EKF approach shows improved robustness giving reasonable good results even for noise levels up to 10% as can be seen in figure 7. In figure 6 the condition number of the matrix $S_k = H_k' P_k^- H_k' T$ which suggests how stable the inversion procedure in the updating step (4) is.

In table 1 the goodness of the reconstructions are shown for each noise level and each algorithm

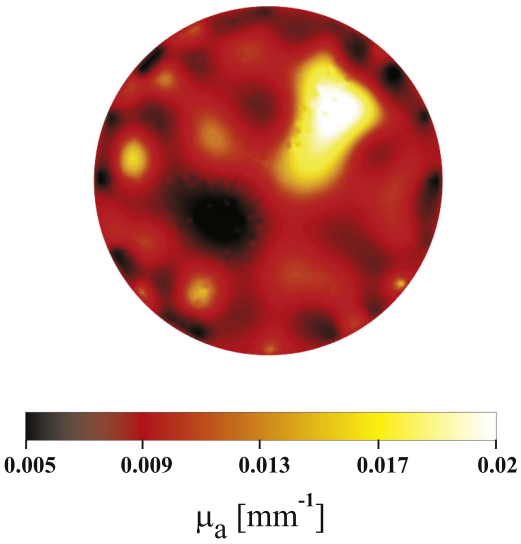

Figure 7. Simulated data reconstruction: reconstruction with a noise level of $\sigma = 10\%$. The goodness for this reconstruction is 0.1653.

Table 1. Goodness of the reconstructions with EKF and NIRFAST.

Noise level $= \sigma$	$e(x_{EKF,\sigma})$	$e(x_{NIRFAST,\sigma})$
$\sigma = 0.005$	0.1236	0.1689
$\sigma = 0.010$	0.1246	0.1722
$\sigma = 0.020$	0.1218	0.2103

Table 2. Comparison of number of iterations and CPU time for scenario 1 reconstructions.

Noise level $= \sigma$	EKF	NIRFAST
$\sigma = 0.005$	3 iterations, 12.10 s	28 iterations, 11.82 s
$\sigma = 0.010$	3 iterations, 11.68 s	23 iterations, 10.54 s
$\sigma = 0.020$	3 iterations, 12.48 s	24 iterations, 10.69 s

according to the merit function given in (13). Note that while NIRFAST inverse solver produces monotonically crescent values of the function $e(x)$, the EKF produces nearly constant values for all three noise levels. This occurs because the EKF was inherently designed to deal with measurement errors [6]. In table 2 iterations and CPU time are shown. The EKF requires less iterations but more time spent at each iteration, this is caused by the line-search procedure at line 7 of algorithm 2. Here, we are using cubic interpolation. Clearly, faster line-search algorithms would result in faster iterations.

In figure 8, we show the reconstruction with the model reduction approach. Although some of the precision is lost, the acceleration is huge given that the amount of nodes is considerably less than our original mesh, the mean time per iteration in the original mesh is about 3.43 s while, on the reduced mesh, the mean iteration time is about 0.43 s, i.e. almost one order of magnitude.

For the experimental data, the reconstruction can be seen in figures 9 and 10 which represents a fifth

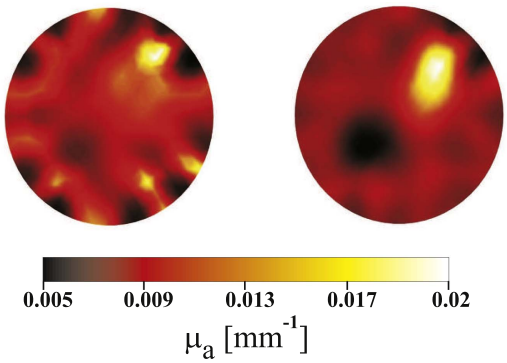

Figure 8. Left: reconstruction without the Model Reduction approach using the coarse mesh with 341 nodes and 618 triangular elements. Right: reconstruction with the Model Reduction approach using the same coarse mesh. The mean iteration time is 0.43 s. The noise level was set to 3 per cent of the maximum value.

iteration of our algorithm, taking 10 min on a 3.9 GHz Pentium I7 and 24 GB of RAM. Regarding the size and location, the inclusions are well recovered, especially with μ_a, although the contrast is not as good as expected in μ_s'. Finally, in μ_s' it is notorious the appearances of artifacts.

7. Discussion and conclusions

In this work, we developed and tested a modified version of the extended Kalman filter (EKF) and applied it to diffuse optical tomography, both in CW and frequency-domain reconstructions. We compared its performance with the NIRFAST inverse solver, obtaining good results concerning robustness. Performed simulations show that the EKF is capable of retrieving both, location and optical properties of embedded inclusions with a certain degree of precision even for noise levels as high as 10%. Moreover, speed is comparable with NIRFAST inverse solver and, additionally, no iteration-based filtering is needed. Given that the EKF produces the Gaussian best approximation the density of the density

$$\pi(x_{k+1}|y_{k+1}) = \exp(-||H(x_{k+1}) - y_k||_R^2 - ||x||_Q^2)/Z \quad (14)$$

where Z is a normalization term, the resulting reconstructions are smooth. Although true solutions may not be smooth, it can be a good starting point for a linear reconstruction which preserves edges, such as L1 or total variation regularization. The covariance matrix obtained may be stored to follow the evolution of the studied media at a later time (for example, to follow the evolution of a lesion or tumor).

The EKF approach can be seen as a generalization of the Gauss–Newton method developed in [15], because of the following two reasons: (i) the EKF contemplates the use of the measurement covariance, which could be obtained via a calibration procedure or

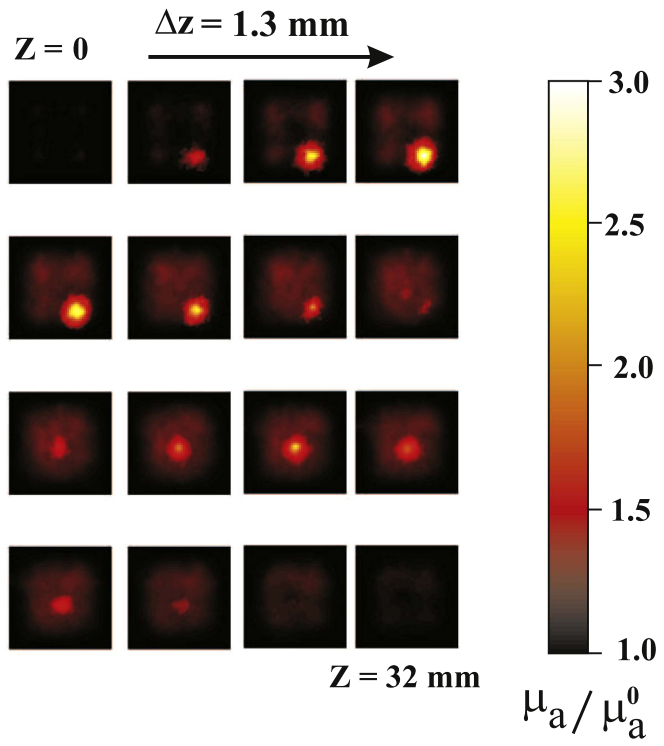

Figure 9. Reconstruction of the relative absorption coefficient from phantom data. From left to right and from top to bottom, the slices of the reconstructed domain in the plane XY. The plane $Z = 0$ corresponds to the slice where the laser impinges on. The separation between consecutive slices is $\Delta z = (33/24)$ mm ≈ 1.3 mm.

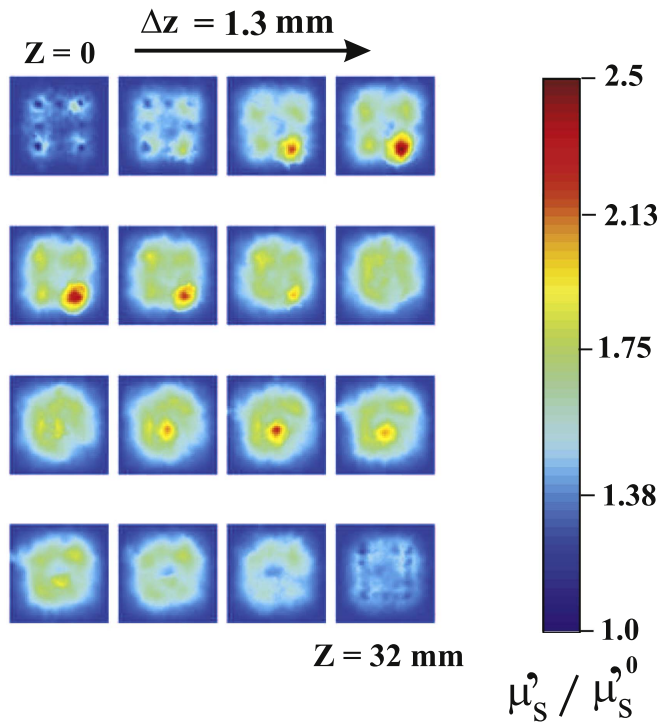

Figure 10. Reconstruction of the relative reduced scattering coefficient from phantom data. It follows the same order as figure 9.

use one as we did in this work inspired by [25]; and (ii) the EKF includes an updating procedure for the parameter (optical properties) covariance matrix.

A drawback of the method is that the memory needed to update the covariance matrix is huge when the size of the mesh is high, but this problem can be tackled when we do not change the covariance over time, assuming that the optical properties covariance are known (for example, a diagonal covariance), or to calculate the covariance in some steps and then stop

updating the covariance matrix, this is equivalent as assuming that the covariance has reached a stationary point, however, this needs to be analyzed further. In some cases, this may be a good approximation considering that many algorithms, so far, make this assumption and perform well. As a matter of fact, in a recent publication [27] reconstructions with full covariance matrix, diagonal variance matrix and identity matrix were performed and compared concluding that the covariance and variance matrix approaches perform similarly but outperform the identity matrix. In practice, this can be achieved by defining the variance matrix without updating the parameter covariance, or, by updating it only in a few iterations and then fixing it.

It is also important to remark that this methodology can be applied to other problems such as Fluorescence Tomography or Difference Tomography by changing model H_k.

As final remarks we would like to mention that: the presented approach could be used or be slightly modified for Functional Monitoring and Imaging by using real measurements at different times instead of fixing as we have done here, which is how the EKF was originally designed for. Another possible approach is to model the evolution of the lesion or tumor and use it in M. Since the EKF is used in many and diverse engineering applications, hardware implementation for actual tomographic devices would be straightforward resulting in faster reconstructions.

8. Funding Information

Authors wish to thank financial support from CONICET, PIP 301 grant and CICPBA, grant FCCIC 2016.

References

[1] Durduran T, Choe R, Baker W B and Yodh A G 2010 *Rep. Prog. Phys.* **73** 076701
[2] Guven M, Yazici B, Intes X and Chance B 2005 *Phys. Med. Biol.* **50** 2837
[3] Yamashita O, Shimokawa T, Aisu R, Amita T, Inoue Y and aki Sato M 2016 *NeuroImage* **135** 287–99
[4] Dehghani H, Eames M E, Yalavarthy P K, Davis S C, Srinivasan S, Carpenter C M, Pogue B W and Paulsen K D 2008 *Commun. Numer. Methods Eng.* **25** 711–32
[5] Schweiger M and Arridge S 2014 *J. Biomed. Opt.* **19** 040801
[6] Simon D 2006 *Optimal State Estimation: Kalman, H infinity, and Nonlinear Approaches* (New York: Wiley)
[7] Humpherys J, Redd P and West J 2012 *SIAM Rev.* **54** 801–23
[8] Diamond S G, Huppert T J, Kolehmainen V, Franceschini M A, Kaipio J P, Arridge S R and Boas D A 2005 Physiological system identification with the Kalman filter in diffuse optical tomography *Medical Image Computing and Computer-Assisted Intervention-MICCAI 2005* (Berlin: Springer) pp 649–56
[9] Alacam B, Yazici B, Intes X, Nioka S and Chance B 2008 *Phys. Med. Biol.* **53** 837
[10] Alacam B, Yazici B, Intes X and Chance B 2006 *IEEE Trans. Biomed. Eng.* **53** 1861–71
[11] Ishimaru A 1978 *Wave Propagation and Scattering in Random Media* (New York: Academic)
[12] Liemert A and Kienle A 2013 *Sci. Rep.* **3** 1-7
[13] Liemert A and Kienle A 2011 *Phys. Rev.* A **83** 015804
[14] Arridge S R 1999 *Inverse Problems* **15** R41
[15] Schweiger M, Arridge S R and Nissil I 2005 *Phys. Med. Biol.* **50** 2365
[16] Contini D, Martelli F and Zaccanti G 1997 *Appl. Opt.* **36** 4587–99
[17] Kienle A 2005 *J. Opt. Soc. Am.* A **22** 1883–8
[18] Kienle A and Patterson M S 1997 *J. Opt. Soc. Am.* A **14** 246–54
[19] Fang Q and Boas D A 2009 *Opt. Express* **17** 20178–90
[20] Kalman R E 1960 *J. Fluids Eng.* **82** 35–45
[21] Golub G H and Van Loan C F 2012 *Matrix Computations* vol 3 (Baltimore: JHU)
[22] Sun W and Yuan Y X 2006 *Optimization theory and methods: nonlinear programming* vol 1 (New York: Springer)
[23] Arridge S R, Kaipio J P, Kolehmainen V, Schweiger M, Somersalo E, Tarvainen T and Vauhkonen M 2006 *Inverse Problems* **22** 175
[24] Vo-Dinh T 2014 *Biomedical Photonics Handbook: Biomedical Diagnostics* vol 2 (Boca Raton, FL: CRC Press)
[25] Ye J C, Bouman C, Webb K and Millane R 2001 *IEEE Trans. Image Process.* **10** 909–22
[26] Kaipio J and Somersalo E 2006 *Statistical and Computational Inverse Problems* vol 160 (New York: Springer)
[27] Brigadoi S, Powell S, Cooper R J, Dempsey L A, Arridge S, Everdell N, Hebden J and Gibson A P 2015 *Biomed. Opt. Express* **6** 4719–37